

Observation Timelines for the Potential Lunar Impact of Asteroid 2024 YR₄

YIFAN HE,¹ YIXUAN WU,¹ YIFEI JIAO,^{1,2} WEN-YUE DAI,^{1,3} XIN LIU,⁴ BIN CHENG,¹ AND HEXI BAOYIN^{1,5}

¹ Tsinghua University, Beijing 100084, China

² Department of Earth and Planetary Science, University of California, Santa Cruz, CA 95064, USA

³ National Astronomical Observatory of Japan, 2-21-1 Osawa, Mitaka, Tokyo 181-8588, Japan

⁴ Nanjing University, Nanjing 210023, Jiangsu, China

⁵ Inner Mongolia University of Technology, Hohhot 010051, China

ABSTRACT

The near-Earth asteroid 2024 YR₄—a \sim 60 m rocky object that was once considered a potential Earth impactor—has since been ruled out for Earth but retained a \sim 4.3% probability of striking the Moon in 2032. Such an impact, with equivalent kinetic energy of \sim 6.5 Mt TNT, is expected to produce a \sim 1 km crater on the Moon, and will be the most energetic lunar impact event ever recorded in human history. Despite the associated risk, this scenario offers a rare and valuable scientific opportunity. Using a hybrid framework combining Monte Carlo orbital propagation, smoothed particle hydrodynamics (SPH) impact modeling, and N-body ejecta dynamics, we evaluate the physical outcomes and propose the observation timelines of this rare event. Our results suggest an optical flash of visual magnitude from -2.5 to -3 lasting several minutes directly after the impact, followed by hours of infrared afterglow from \sim 2000 K molten rock cooling to a few hundreds K. The associated seismic energy release would lead to a global-scale lunar reverberation (magnitude \sim 5.0) that can be detectable by any modern seismometers. Furthermore, the impact would throw out $\sim 10^8$ kg debris to escape the lunar gravity, with a small fraction reaching Earth to produce a lunar meteor outburst within 100 years. Finally, we integrate these results into a coordinated observation timeline, identifying the best detection windows for ground-based telescopes, lunar orbiters and surface stations.

Keywords: Near-Earth objects (1092) — Impact phenomena (779) — Monte Carlo methods (2238) — Ejecta (453) — Lunar impacts (958)

1. INTRODUCTION

Asteroid 2024 YR₄ was discovered in late 2024 as a \sim 60 m Apollo-class near-Earth asteroid (B. T. Bolin et al. 2025; A. Rivkin et al. 2025) whose orbit crosses those of both Earth and the Moon. Refined orbital solutions in mid-2025 (NASA 2025) indicate a 4.3% probability that 2024 YR₄ will strike the Moon on 2032 December 22 at a velocity of \sim 14.1 km s⁻¹. Should this occur, 2024 YR₄ would deliver a kinetic energy of $\sim 3 \times 10^{16}$ J—about 6.5 megatons of TNT—excavating a \sim 1 km-scale crater with a depth of \sim 150 m. Such an event would constitute the most energetic lunar impact in several millennia and an unprecedented natural experiment in impact physics.

Only far smaller lunar impacts have ever been directly observed. For example, the 2013 September 11 event

(J. M. Madiedo et al. 2014), produced by a \sim 400 kg meteoroid, generated a brief 3rd-magnitude flash and a crater only 40 meters wide. The 2024 YR₄ impact, by contrast, would release energy 6 orders of magnitude greater—comparable to a medium nuclear detonation—and would trigger a suite of observable phenomena: an intense optical and infrared flash, a km-scale melt pool, a global moonquake, and a short-lived cloud of escaping ejecta. Historical Apollo seismometers recorded even the \sim 1 kT TNT-equivalent impact of the Apollo 13 S-IVB stage at global distances (T. Gudkova et al. 2011), implying that a 2024 YR₄-sized collision would produce seismic signals readily detectable across the Moon. Moreover, the fastest ejecta could exceed the lunar escape speed, temporarily populating cislunar space and, within days, producing a meteoroid flux toward Earth—raising both scientific interests and hazard considerations for artificial satellites, as discussed in ?.

Here we present a comprehensive analysis of the dynamical, thermal, and seismic consequences of a potential 2024 YR₄ impact and evaluate their observability across multiple domains. Our study combines high-precision Monte Carlo orbital propagation (X. Liu et al. 2025) with smoothed particle hydrodynamics (SPH) impact simulations (Y. Jiao et al. 2024a) and N-body modeling of high-velocity ejecta (H. Rein & S.-F. Liu 2012). From these results we derive quantitative predictions for the optical flash, crater formation, ejecta dispersion, thermal afterglow, and seismic wave amplitudes, linking each to specific observational platforms and timescales. We further integrate these outcomes into a coordinated observation framework encompassing ground-based telescopes, lunar orbiters, surface seismometers, and space-based assets, summarized in a unified timeline of detectability. Our work emphasizes the full chain of observable effects—from the sub-second optical flash to the multi-day infrared emission and global seismic response—and outlines how simultaneous monitoring across these domains could yield the most complete dataset ever obtained for a large lunar impact. If the predicted collision indeed come up, 2024 YR₄ will offer a once-in-a-generation opportunity to observe, in real time, the interplay between impact dynamics, lunar geology, and near-Earth space environment, providing crucial benchmarks for planetary-defense modeling and future lunar science.

2. METHODOLOGY

2.1. Monte Carlo Orbit Sampling and Impact Geometry

To better constrain the impact corridor and simulation parameters, we generated 10^4 orbit “clones” by sampling the 6×6 covariance of the nominal JPL/MPC solution (NASA/JPL Small-Body Database 2025; Minor Planet Center 2024) (mid-2025) for 2024 YR₄.

Each clone’s Cartesian state at epoch was drawn from the covariance ellipsoid and numerically propagated to 2032 December using a high-precision N-body integrator with relativistic terms, DE441 ephemerides for all major bodies (Sun, eight planets, Pluto, Earth–Moon resolved; lunar gravity consistent with DE441), and an adaptive Radau/Prince–Dormand scheme with absolute tolerance 10^{-12} and base step ~ 0.1 d. Nongravitational forces were neglected over the 7–8 yr horizon (X. Liu et al. 2025). A “lunar impact” is flagged when a trajectory crossed the lunar radius plus gravitational focusing.

From this single Monte Carlo campaign, we directly obtain the key impact statistics and geometry: 426/10,000 clones intersect the Moon on 2032-12-22, implying $P_{\text{imp}} = 4.26\%$. Impact times cluster within

2 hours of 15:18 UTC. All impacts occur at $v_{\text{imp}} = 14.1 \text{ km s}^{-1}$ with $< 0.01\%$ dispersion; incidence angles span $36^\circ – 88^\circ$ (from vertical). The resulting impact corridor is shown in Figure 1. These consolidated outcomes are used directly to select angles and speed for impact modeling below.

2.2. SPH Impact Simulation

We simulate the impact process with SPH simulations for 500 s from the collision instant (Y. Jiao et al. 2024a,b). Because the size of 2024 YR₄ (tens of meters) is far less than the Moon, the impact affects only a local region of the surface. Accordingly, the computational domain is taken as a hemispherical region of 3 km diameter centered on the impact point where $\sim 6 \times 10^6$ particles are adopted, with lunar gravity approximated as a constant $g_{\text{Moon}} = 1.625 \text{ m s}^{-2}$.

The projectile is modeled as a 60 m rocky sphere (S-type proxy) at $v_{\text{imp}} = 14.1 \text{ km s}^{-1}$ impacting into a local half-space of lunar regolith. Three representative incidences ($36^\circ, 60^\circ, 84^\circ$) are consistent with the Monte Carlo geometry. The material response is modeled using the Lund strength model, the Tillotson equation of state, and the p - α porosity compaction model. For the lunar surface, the shallow regolith layer is treated as a fully damaged, loosely consolidated granular medium with finite cohesion (G. S. Collins et al. 2004; M. Jutzi 2015). The basaltic material parameters are adopted for the equation of state (H. Melosh 1989), and the porosity model parameters follow the analysis of M. Jutzi et al. (2008, 2009). The projectile (2024 YR₄) is described by a von Mises strength model with a yield strength of 100 MPa (B. Cheng & H. Baoyin 2024) and the Tillotson EOS for basalt.

All material parameters applied in our simulations are summarized in Table 1. The outcomes of our simulations are the transient/final crater dimensions, ejecta speed/angle distributions (including the high-velocity tail), and diagnostic fields (pressure, damage).

2.3. High-Velocity Ejecta Evolution

To model the orbital fate of escaping fragments, we construct six launch cases, corresponding to two representative points along the lunar impact corridor for each of the three incidence angles ($36^\circ, 60^\circ, 84^\circ$). For each case, test particles are released from the lunar surface within a conical launch geometry of half-angle 45° , following the ejecta pattern in our impact simulation. The truncated power-law distribution of a particle swarm with a total number of N_0 is derived from the SPH outputs and approximated by

$$N(>v) \propto v^{-\gamma}. \quad (1)$$

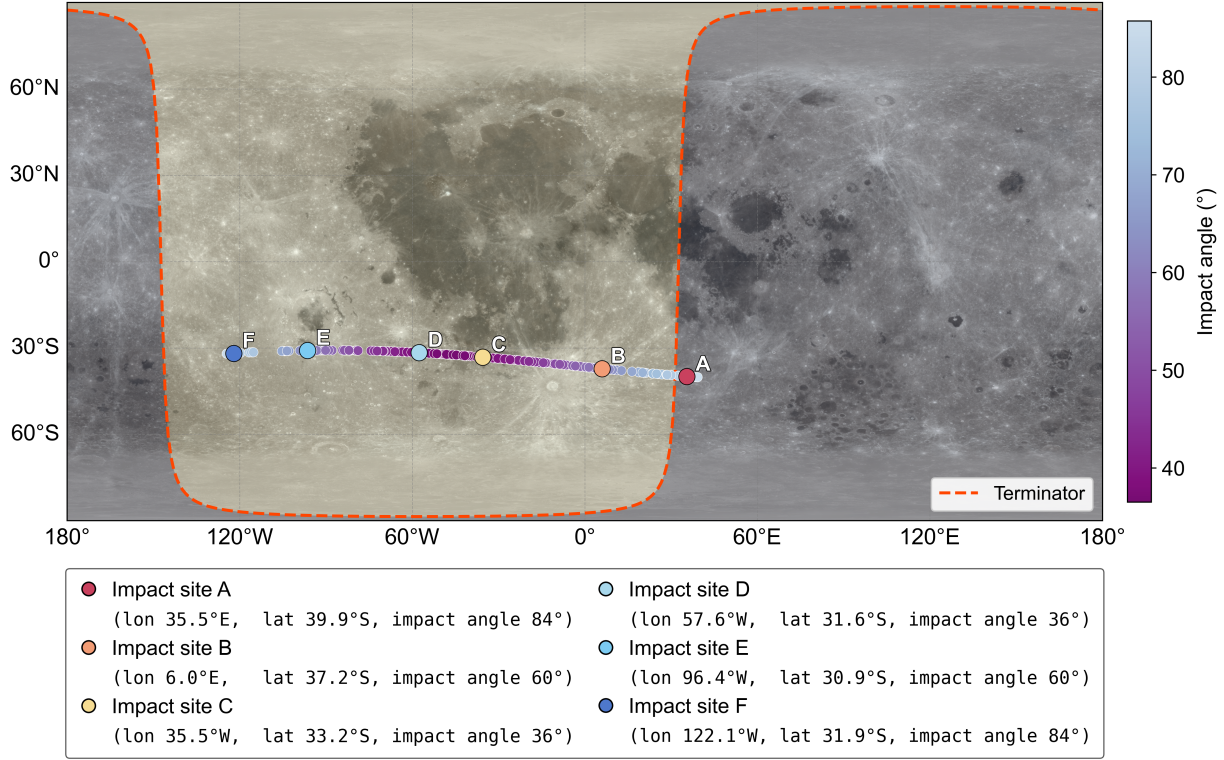


Figure 1. Map of the Moon’s entire surface showing the 4.3% 2024 YR₄ impact corridor (with impact angle) and the dawn/dusk terminator (orange) on 22 December 2032 at 15:19 UTC. Six representative impact sites are highlighted, with their coordinates and impact angles listed in the bottom legend.

Table 1. SPH material parameters adopted for the 2024 YR₄ lunar impact simulations

Material	ρ_0 (kg m ⁻³)	A_t (GPa)	B_t (GPa)	a_t	b_t	α_t	β_t	E_0 (MJ kg ⁻¹)	E_{iv} (MJ kg ⁻¹)	E_{cv} (MJ kg ⁻¹)	Y_{i0} (Pa)	Y_{d0} (Pa)	Y_m (Pa)	μ
Lunar regolith (shallow)	3400	26.7	26.7	0.5	1.5	5.0	5.0	487	18.2	4.72	—	1.0×10^3	1.0×10^9	0.6
Asteroid 2024 YR ₄	2700	26.7	26.7	0.5	1.5	5.0	5.0	487	18.2	4.72	1.0×10^8	0	3.5×10^9	0.8

NOTE— ρ_0 initial density; A_t , B_t Tillotson coefficients; a_t , b_t , α_t , β_t dimensionless EOS parameters; E_0 , E_{iv} , E_{cv} specific energies; Y_{i0} , Y_{d0} , Y_m strength terms; μ internal friction.

For each launch site, we perform Monte Carlo realizations of 20,000 particles, drawing velocity magnitudes from the above distribution and azimuths randomly within the cone signed in Figure 1.

The particles are mapped into Earth–Moon barycentric inertial states at the instant of launch and propagated using the N-body simulation code REBOUND (H. Rein & S.-F. Liu 2012). During the 100-year orbital evolution, particles are advanced in a full heliocentric model including the Moon and all eight planets. Non-gravitational perturbations are neglected, as the solar radiation pressure is less than 10^{-3} of Earth’s gravity at the lunar distance for the minimum fragment size considered ($D \sim 1$ mm) (J. A. Burns et al. 1979; P. Wiegert

et al. 2025; Y. Yu et al. 2017). Each particle is treated as massless in the N-body integration, but representative sizes and masses are assigned post-facto according to a cumulative power-law size–frequency distribution of escaping fragments. The size distribution is written as

$$N(> D) = N_{0,D} D^{-\beta} \quad (2)$$

where the index β is about 3.4–3.6 according to SPH simulations (Y. Jiao et al. 2024b). We adopt an upper cutoff diameter of $D_{\max} \approx 2$ m, corresponding to ~ 0.035 times the diameter of 2024 YR₄ (Y. Wu et al. 2025). $N_{0,D}$ is taken to match the total mass of escape ejecta in each case. This provides a quantitative mapping between the dynamical test particles and the

physical ejecta population. We record orbital states and collisions with large bodies of all ejecta. This setup thus links SPH-derived crater-scale ejection kinematics to the longer-term dispersal and impact fates of 2024 YR₄ ejecta.

3. RESULTS

3.1. SPH Impact Simulation Results

Shown in Figure 2, in every case, 2024 YR₄ produces a simple bowl-shaped crater with a km-scale diameter, consistent with analytic scaling by G. Collins et al. (2011) and B. Cheng et al. (2018). At 36° incidence, the crater stabilizes at ~ 1.4 km diameter and ~ 260 m depth, forming a circular bowl. The ejecta rays are radially distributed with no pronounced asymmetry. At 60°, the crater reaches ~ 1.0 km diameter and ~ 150 m depth ($d/D \simeq 0.15$). The ejecta blanket displays a butterfly-shaped asymmetry, with rays extending tens of crater radii preferentially downrange. At the most oblique (84°) incidence, the crater is smaller (~ 0.6 km) and shallower (120 m); its horizontal section is elliptic with axis ratio ~ 0.83 , and ejecta are sparse, confined to two lateral sectors with no coherent ray texture. These morphologies match established oblique impact systematics (X.-Z. Luo et al. 2022).

The total mass of high-velocity ejecta escaping the Moon (exceeding 2.37 km s⁻¹) varies strongly with impact angle either. At the 36° incidence (i.e., Craters C and D), the impact produces the most energetic ejection, yielding a total escaping mass of $\sim 2.44 \times 10^8$ kg. The 60° case (i.e., Crater B and E) ejects about 1.94×10^8 kg above the lunar escape speed, while the most oblique 84° impacts (i.e., Craters A and F) generate only $\sim 3.53 \times 10^7$ kg of escaping fragments. The impact simulations were further used to fit the velocity–frequency power-law slopes of the escaping ejecta, yielding $\gamma \simeq 1.01, 0.87$, and 0.38 for 36°, 60°, and 84°, respectively.

3.2. Impact Flash and Thermal Afterglow

The luminous output of a hypervelocity lunar impact is estimated by scaling the kinetic energy with a luminous efficiency η (G. Merisio & F. Topputto 2023):

$$E_{\text{vis}} = \eta E_{\text{imp}}. \quad (3)$$

Laboratory and lunar flash monitoring suggest $\eta \sim 10^{-3}$ – 10^{-2} (J. M. Madiedo et al. 2014; M. Ait Moulay Larbi et al. 2015); here we explore the higher end ($\eta = 10^{-2}$) to assess the bright-flash regime, justified by the relatively large size and rocky composition of 2024 YR₄. For $E_{\text{imp}} \sim 3 \times 10^{16}$ J, this gives $E_{\text{vis}} \simeq 3 \times 10^{14}$ J released as visible/near-IR radiation.

The time dependence of the flash can be abstracted by an effective duration τ_{eff} defined as

$$E_{\text{vis}} = \int_{-\infty}^{+\infty} \phi(t) dt, \quad \tau_{\text{eff}} \equiv \frac{E_{\text{vis}}}{\phi_{\text{pk}}}, \quad (4)$$

where $\phi(t)$ is the instantaneous radiant power and ϕ_{pk} its peak. If the lightcurve has total duration T and a shape factor χ (e.g., $\chi = 1$ for a rectangular pulse, $\chi = 2$ for a triangular pulse), then

$$\tau_{\text{eff}} = \frac{T}{\chi}, \quad \phi_{\text{pk}} = \chi \frac{E_{\text{vis}}}{T}. \quad (5)$$

The peak flux at Earth is then defined as $F_{\text{pk}} = \frac{\phi_{\text{pk}}}{4\pi\Delta^2}$, with Δ as the Earth–Moon distance. Restricting to the V band, with fractional energy f_V of the spectrum and zero-point flux $F_{V,0}$, the apparent peak magnitude is

$$m_V = -2.5 \log_{10} \left(\frac{F_{V,\text{pk}}}{F_{V,0}} \right), \quad F_{V,\text{pk}} = f_V F_{\text{pk}}. \quad (6)$$

Applying this framework with $E_{\text{vis}} \sim 3 \times 10^{14}$ J and $T \sim 100$ – 1000 s yields $\phi_{\text{pk}} \sim 10^{11}$ – 10^{12} W, giving a peak flux at Earth of order 10^{-7} – 10^{-6} W m⁻² and an apparent magnitude $m_V \simeq -2.5$ – -3 . To estimate the exact duration of the flash, we adopt the empirical equation (J. M. Madiedo et al. 2015)

$$\tau = (77.6 \pm 34.4) \exp[-(0.94 \pm 0.06) m_V], \quad (7)$$

which for $m_V \simeq -2.5$ – -3 gives a duration of ~ 300 – 2000 s, consistent with our initial assumption.

The spectral peak is near 1.2–1.6 μm , corresponding to blackbody temperatures of 1800–2300 K. The spectral radiance of a blackbody (S. Bouley et al. 2012) is

$$L(\lambda, T) = \frac{2\pi hc^2}{\lambda^5} \left[\exp\left(\frac{hc}{\lambda k_B T}\right) - 1 \right]^{-1}, \quad (8)$$

and the effective temperature T_{eff} is constrained by the energy balance

$$\frac{P_0}{\beta\pi R^2} = \int_{\lambda_1}^{\lambda_2} L(\lambda, T_{\text{eff}}) d\lambda, \quad (9)$$

where P_0 is the peak radiant power, β is a geometric correction factor, R is the effective source radius, and (λ_1, λ_2) denote the observational bandpass (here 0.4– $0.9 \mu\text{m}$). Applying this relation yields $T_{\text{eff}} \sim 1800$ – 2300 K, consistent with the near-IR peak.

Following the plasma flash, shock heating produces a ~ 100 m melt pool at $T \sim 2000$ K. Radiative cooling calculations predict an infrared afterglow detectable for hours to days: effective temperatures decline from

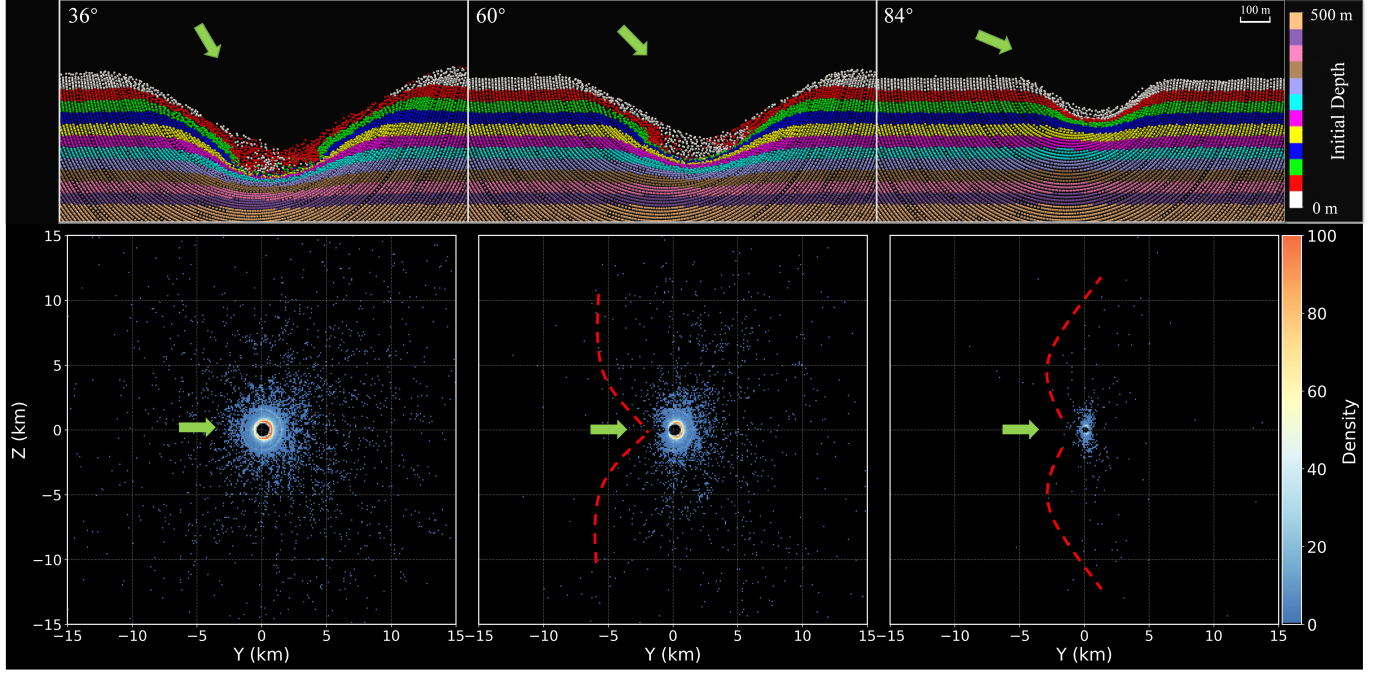


Figure 2. SPH outcomes for three incidence angles (36° , 60° , 84°). Top row: crater cross-sections at late time ($t \sim 200$ s) showing size and depth differences. Bottom row: plan-view ejecta patterns on the lunar surface, illustrating transition from near-radial symmetry at 36° , to asymmetric butterfly rays at 60° , then to sparse wing-shaped ejecta landing points at 84° . The central black area marks the impact crater, and the region to the left of the red dashed line denotes the zone of avoidance (ZoA) with no ejecta relatively.

~ 1500 K to ~ 500 K within several hours, but remain elevated ($\gtrsim 300$ K) for 1 to 2 days. Such a km-scale anomaly would be accessible to infrared instruments on LRO/Diviner or large-aperture ground-based telescopes during lunar night.

3.3. Seismic Shock and Moonquake

A fraction of the impact energy transforms into seismic waves that cause shallow moonquakes with large magnitudes (C. Nunn et al. 2020). Following empirical scaling, the seismic energy is

$$E_{\text{seismic}} = k E_{\text{imp}}, \quad (10)$$

with efficiency $k \sim 10^{-4}$. For 2024 YR₄ ($E_{\text{imp}} \sim 3 \times 10^{16}$ J), this gives $E_{\text{seismic}} \sim 3 \times 10^{12}$ J. The corresponding seismic magnitude can be estimated from the Gutenberg–Richter relation (H. Melosh 1989)

$$M_{\text{seismic}} = \frac{2}{3} \log_{10} E_{\text{seismic}} - 3.2, \quad (11)$$

which yields $M_{\text{seismic}} \simeq 5.0\text{--}5.1$.

Impact-induced seismic waves include compressional (P) and shear (S) body waves as well as surface Rayleigh waves. Because the Moon’s liquid core and fractured crust strongly attenuate S-wave propagation, surface waves dominate the observable ground motion. For a

given impactor impulse mU , the acceleration spectral density of the body waves can be estimated empirically (C. Nunn et al. 2024) as

$$A_{\text{seismic}} = 1.1 \times 10^{-12} S m U f^3 / D, \quad (12)$$

where A_{seismic} is in $\text{m s}^{-2} \text{Hz}^{-1/2}$, S is the seismic amplification (typically $S \sim 1.7$), mU is the impactor momentum (kg m s^{-1}), f is the frequency (Hz), and D is the epicentral distance (m).

To estimate far-field Rayleigh-wave amplitudes from the impact source, we adopt the standard cylindrical geometric-spreading and anelastic-attenuation form (K. Aki & P. G. Richards 2002; H. Sato et al. 2012):

$$A(r, f) = A_0(f) r^{-1/2} \exp\left[-\frac{\pi f r}{Q_R v_R}\right], \quad (13)$$

where $A_0(f)$ is the source amplitude at frequency f , v_R is the Rayleigh-wave speed ($\simeq 2.6 \text{ km s}^{-1}$), and $Q_R \sim 10^3$ is the quality factor of the lunar crust (J.-F. Blanchette-Guertin et al. 2012; R. F. Garcia et al. 2011). The corresponding peak ground velocity (PGV) at a seismic station is

$$\text{PGV}(r, f) = \text{PGV}_0(f) r^{-1/2} \exp\left[-\frac{\pi f r}{Q_R v_R}\right], \quad (14)$$

where $\text{PGV}_0(f)$ is the near-source reference amplitude. These relations enable estimation of the signal strength

at any lunar seismometer as a function of frequency and distance from the impact site.

The combined models indicate that even at farside distances ($r \gtrsim 1500$ km), 2024 YR₄-type impacts would generate surface-wave velocities above 10^{-6} m s⁻¹, readily detectable by current or planned lunar seismometers. Because of the Moon's low attenuation and scattering, reverberations may persist for tens of minutes. Near the impact, ground motion would be extreme; globally, spectral amplitudes remain above Apollo noise levels, ensuring detection by any sensitive station. Secondary processes such as ejecta fallback and distal secondary impacts could also inject transient seismic energy. Overall, the predicted $M \sim 5$ moonquake would rank among the strongest modern lunar seismic events, providing a rare opportunity to probe crustal structure, attenuation, and energy coupling in the lunar interior.

3.4. Evolution of Escaped Lunar Ejecta

The 2024 YR₄ impact is expected to eject 10^7 – 10^8 kg of lunar material that escapes the Moon (Section 3.1), generating a stream of particles from millimeter-sized meteoroids to meter-scale boulders. Our orbital simulations reveal the diverse dynamical fates of these ejecta and highlight their strong dependence on the impact location on the Moon.

3.4.1. Lunar ejecta flux to Earth

For an impact on the lunar trailing side (i.e., Craters A and B), the dynamics favor a high Earth-delivery efficiency. Although the high impact angles (60° – 84°) limit the total ejecta mass, the debris is launched with lower geocentric velocities, facilitating a rapid transfer. The first wave of particles arrives within 2–8 days, delivering $\sim 1\%$ of the total mass immediately. Based on the size distribution in Eq. (2), the total ejecta mass (4×10^7 – 2×10^8 kg) yields up to 10^{13} meteoroids (> 1 mm), corresponding to an average naked-eye flux of ~ 1 – 6×10^5 hr⁻¹. Furthermore, we estimate a fireball rate of 100–400 hr⁻¹, considering the luminosity expected at an entry speed near Earth's escape velocity as derived from our orbital simulations (Z. Ceplecha et al. 1998; D. Subasinghe & M. Campbell-Brown 2018). This intensity represents a historic storm posing severe hazards to satellites, a conclusion consistent with P. Wiegert et al. (2025). Following this initial burst, the flux peaks again at ~ 30 and ~ 90 days post-impact, with a cumulative 5–6% of the escaped lunar debris entering Earth's atmosphere over 100 years.

In contrast, the latest orbit determination of 2024 YR₄ places the potential impact primarily on the Moon's leading side (i.e., Craters C–F). Ejecta from the leading side have higher geocentric velocities, causing a larger

fraction to escape the Earth–Moon system (Figure 3c) and reducing the Earth-delivery efficiency by an order of magnitude relative to the trailing side. The earliest meteoroids reach Earth after ~ 80 days, and Earth accretes only $\sim 1\%$ of the total mass over 100 years, which is comparable to the first-week delivery fraction from a trailing-side impact. Notably, the leading-side impact cases of 2024 YR₄ are generally less oblique and could release more than 2×10^8 kg of ejecta, producing a meteor shower of up to 2×10^7 hr⁻¹ starting 80 days post-impact, despite the lower delivery ratio (Figure 3a).

3.4.2. Predicted Lunar Meteorite Delivery

The ejecta flux includes 50–350 boulders of meter-sized (derived from Eq. (2), corresponding to a total escaping mass of 10^5 – 10^6 kg) that escape the Moon, depending on the impact location. Upon entering Earth's atmosphere, these objects undergo catastrophic disruption, potentially yielding surviving meteorite masses of 0.1–3% of the pre-atmospheric mass (O. Popova et al. 2011).

By combining the initial boulder yield with the Earth-delivery probability derived from our orbital simulations, we map the expected meteorite fall flux within the first two years after the impact, projected onto a standard world map¹ (Figure 4). The lunar trailing side (i.e., Craters A and B) offers the greatest potential for sample recovery due to its superior transport efficiency. Specifically, an impact on Crater B maximizes the yield, delivering a total meteorite mass of ~ 400 kg within the first year. Conversely, impacts on the leading side (i.e., Craters C–F) result in a significantly lower yield, estimated at $\lesssim 20$ kg over the same period, despite the potentially larger initial ejecta mass.

The simulations show that meteorite falls occur across all latitudes, confirming potential falls in Antarctica, which remains a prime location for meteorite recovery (U. B. Marvin 1983). For the maximum-yield scenario (Crater B), the fallout concentrates along a diagonal band that extends across South America, North Africa, and the Arabian Peninsula. These regions contain extensive arid environments that are highly favorable for future search campaigns, offering a unique opportunity to recover samples with definite geological provenance.

3.4.3. Secondary impacts on the Moon

While some lunar ejecta strike Earth, others remaining bound to the Earth–Moon system may subsequently re-impact the Moon as they cross its orbital plane (Figure 3b). Re-impact probabilities depend strongly on the

¹ Standard Map Service, Map Approval No. GS(2016)1665.

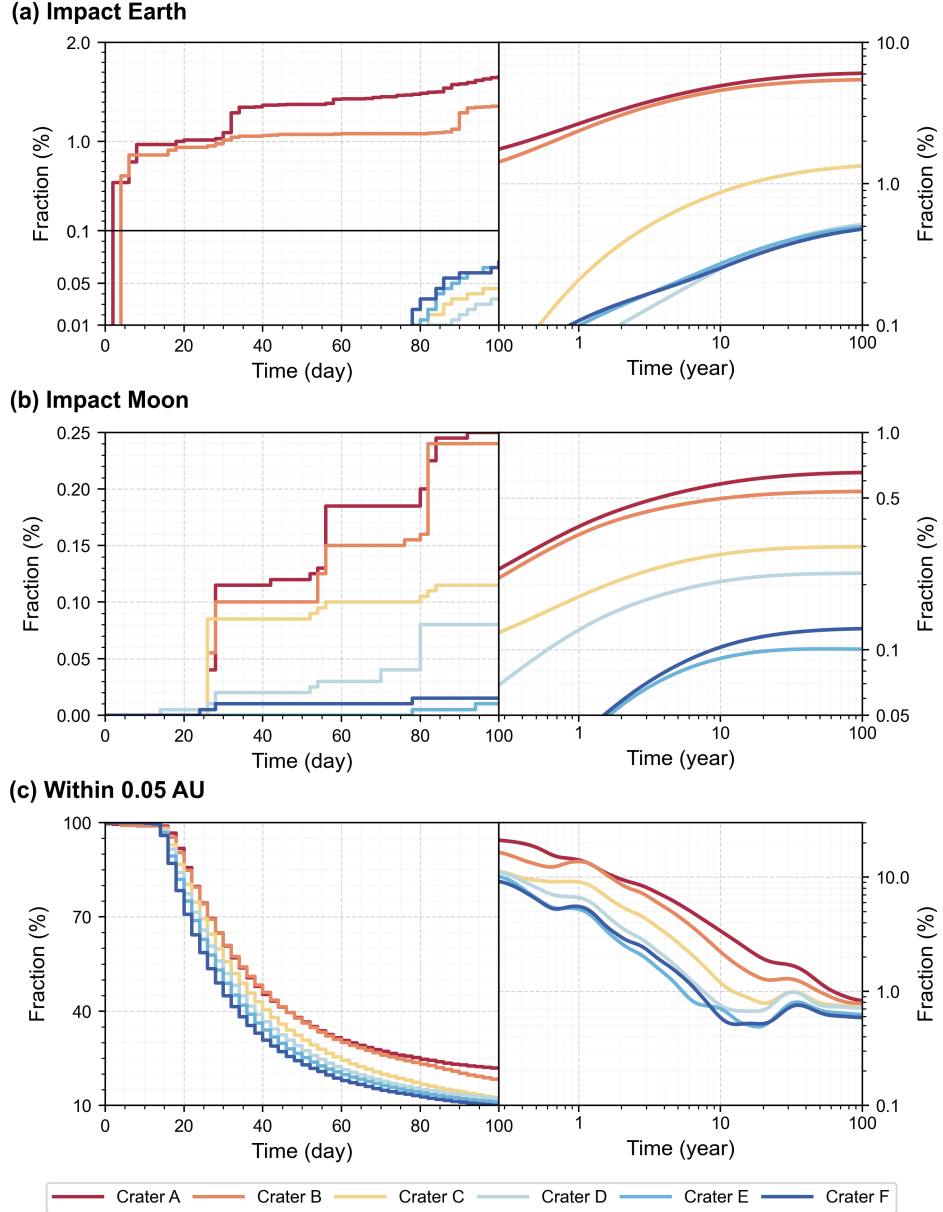


Figure 3. Time evolution of ejecta fractions impacting Earth (a) and the Moon (b), or remaining within 0.05 AU of Earth (c). The time axis is split into linear (first 100 days) and logarithmic (up to 100 yr) scales. In (a), the left panel uses a broken y-axis to better display the low fractions from Craters C–F.

source location, peaking at $\sim 0.25\%$ (within 100 days) for trailing-side ejecta while dropping significantly for the leading side. The secondary impacts exhibit monthly peaks, a periodicity arising from fragments in geocentric orbits with near-lunar periods that repeatedly encounter the Moon at their orbital nodes. Over 100 years, the cumulative re-impact mass is less than double the first-year value, indicating a strong concentration at early times.

With an assumed luminous efficiency of 2×10^{-3} , secondary impacts may produce observable optical flashes when their kinetic energy exceeds 10^6 J, which corre-

sponds to the ~ 11.2 mag detection limit of NELIOTA (E. Xilouris et al. 2018). Our orbital simulations, weighted by the ejecta size distribution, show that an impact on the trailing side (e.g., Crater B) produces $\gtrsim 2000$ observable flashes within the first year. In contrast, impacts on the leading side show widely varying results: Craters C and D account for ~ 800 –1200 secondary flashes, while Craters E and F yield fewer than 200. Beyond these orbital returns, the prompt fallback of massive, non-escaping fragments is expected to trig-

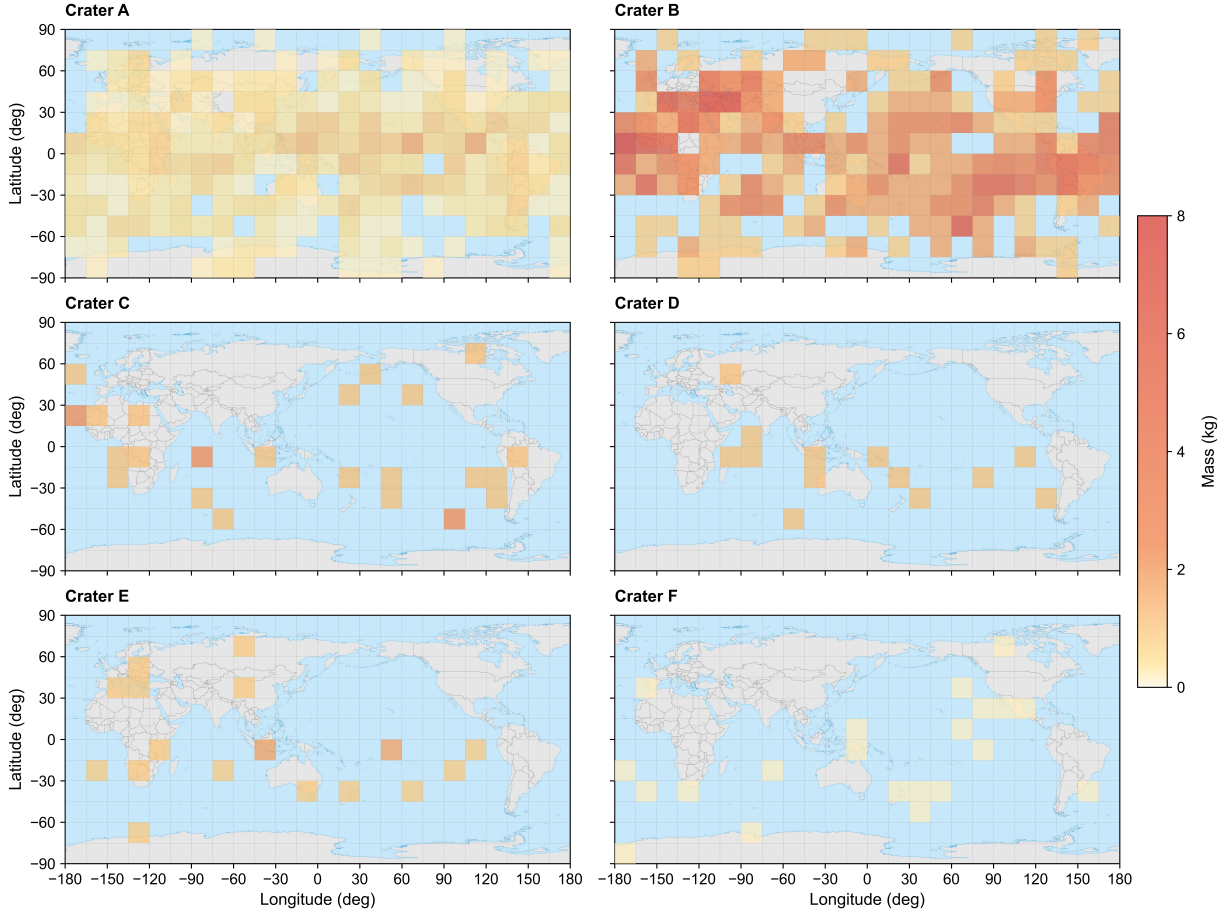


Figure 4. Predicted global distribution of surviving meteorite mass delivered to Earth over the first two years post-impact (T_0 to $T_0 + 2$ yr). The panels map the expected cumulative mass within each grid cell, projected onto a standard world map, for the six source craters.

ger numerous additional flashes immediately following the main impact.

3.4.4. Detectability of meter-scale boulders

Within the first 100 days, the fraction of ejecta remaining in Earth’s vicinity (<0.05 AU) drops to 10–20%. During the following century, this fraction gradually decreases and levels off at $\sim 1\%$, reflecting a dynamic equilibrium between fragments drifting away and their returning (Figure 3c). This remaining fraction corresponds to a substantial population of meter-scale boulders near Earth, motivating us to assess their detectability with current surveys.

The Legacy Survey of Space and Time (LSST) can detect trailed sources down to magnitude ~ 24 with angular velocities up to ~ 10 deg day $^{-1}$ (Y. Wu et al. 2025; Z. Ivezić et al. 2019). We estimate the number of detectable 1–2 m boulders, assuming a minimum 10-day observational arc. In high-yield scenarios (Craters B–E), LSST is expected to identify a total of 20–50 distinct objects over 100 years post-impact, whereas lower-yield

cases (Craters A and F) produce $\lesssim 10$. Among these detectable targets, the majority are observed while bound to Earth (distance < 0.01 AU, geocentric energy < 0). This fraction exceeds 60% in all cases (averaging $\sim 75\%$) and reaches $> 80\%$ for the trailing-side craters. While most detections ($\sim 70\%$ averaged across all craters) occur within the first year, a distinct subset ($> 10\%$) is identified upon returning from heliocentric orbits 50–100 years later, indicating that the 2024 YR₄ impact leaves an enduring observational signature in near-Earth space. Crucially, our simulations indicate that $\sim 70\%$ of these targets overall remain observable for > 0.1 years, allowing extended windows for precise orbit determination.

Extending the survey to the sub-meter regime (0.5–1 m) provides a valuable supplement by increasing the candidate count by a factor of ~ 4 –5. However, the fraction of detectable objects yielding arcs > 0.1 years drops to $\sim 44\%$ at 0.5 m and merely $\sim 7\%$ at 0.3 m, below which detections become negligible.

Table 2. Observability Timeline for the 2024 YR₄ Lunar Impact Event

Observing Platform	Detection Window	Phenomenon	Peak Value	Notes	Science Qs.
Optical Flash Phase					
Earth-based telescopes (≥ 0.3 m)	T_0 to + $\sim 10^3$ s	Optical flash	$m_V \simeq -2.5$ to -3	Visible from Hawaii	Q1 (luminous efficiency, angle/velocity); Q3 (early vapor lines)
Naked-eye observers	T_0 to + ~ 10 s	Optical flash	$m_V \simeq -3$	Brief, star-like burst	Q1 (occurrence, gross energy)
JWST / space telescopes	T_0 to + $\sim 10^3$ s	Optical/NIR flash	$m_{1.6\ \mu\text{m}} \simeq -5$	Coordinate ToO observation	Q1 (radiative partition); Q3 (vapor composition)
Lunar orbiters (e.g., LRO)	T_0 to +hours	Optical/IR plume	Bright transient	Direct line-of-sight required	Q1 (plume kinematics); Q3 (plume-exosphere coupling)
Thermal Infrared Afterglow					
Earth-based IR telescopes	+10 min to +48 h	Thermal afterglow	1500–500 K	Favorable during lunar night	Q3 (thermal inertia/porosity, melt volume); Q1 (cooling energetics)
Space IR (JWST/MIRI)	+min to +days	Thermal emission	1500–300 K	Constrain melt composition	Q3 (emissivity, volatiles)
Lunar orbiters (Diviner, etc.)	+min to +weeks	Surface heating	1500–100 K	High-res thermal crater mapping	Q3 (T(x,y,t), layering, melt geometry); Q1 (obliquity heating asymmetry)
Seismic Shock Phase					
Lunar surface seismometers	T_0 to +hours	P, S, Rayleigh waves	$M_{\text{seismic}} \simeq 5.0\text{--}5.1$	Global detection expected	Q2 (source, Q_s , structure); Q1 (coupling)
CLIPS Far-side Seismic Suite	+8–12.0 min, for 10–30 min	Rayleigh wave	PGV $\simeq 0.17\text{ mm s}^{-1}$	VBB + SP array; easily detectable	Q2 (far-side attenuation/anisotropy)
Artemis LEMS (South Pole)	+11–12 min, for 10–30 min	Rayleigh wave	PGV $\simeq 0.09\text{ mm s}^{-1}$	High S/N; autonomous polar station	Q2 (polar structure, dispersion)
Chang'e 8 lander	+10–13 min, for 10–30 min	Rayleigh wave	PGV $\simeq 0.10\text{ mm s}^{-1}$	Clear signal; seismometer onboard	Q2 (near-side megaregolith)
LUPEX (JAXA-ISRO)	+10–13 min, for 10–30 min	Rayleigh wave	PGV $\simeq 0.10\text{ mm s}^{-1}$	Detectable if seismic package onboard	Q2 (regional Q_s , dispersion)
South-Pole Station (85°S, 0°E)	+8.9 min, for 10–30 min	Rayleigh wave	PGV $\simeq 0.16\text{ mm s}^{-1}$	Broadband; favorable for polar missions	Q2 (polar tomography)
Lunar orbiters with seismic payload	+min to +hours	Orbital acceleration	Moderate	Possible small orbital perturbation	Q2 (long-period response)
Escaped Lunar Ejecta					
Ground meteor networks	+2 d to 100 d	Meteor storm	$\sim 5 \times 10^8\text{ h}^{-1}$	Severe satellite hazard	Q1 (escape fraction, size-speed); Q3 (cislunar dust environment)
Meteorite search campaigns	+weeks to 1 yr	Meteorite falls	$\sim 400\text{ kg (Total)}$	Antarctica/Arid regions	Q3 (shock/volatiles/composition link); Q1 (ejecta provenance)
Flash monitoring (NELIOTA)	+days to months	Secondary impacts	~ 3000 flashes		Q1 (recapture efficiency); Q3 (gardening rate)
Optical wide-field survey (LSST)	0.1 to 100 yr	Boulders ($\sim 1\text{ m}$)	20–50 objects	Accessible mission targets	Q1 (three-body pathways, RP response); Q3 (fresh boulder spectra)

NOTE— T_0 = nominal impact epoch (2032 Dec 22 15:19 UTC). Optical/IR parameters assume $E_{\text{seismic}} = kE_{\text{imp}}$ with $k = 10^{-4}$ and Rayleigh-wave attenuation

$\text{PGV}(r, f) = \text{PGV}_0(f) r^{-1/2} \exp[-\pi f r / (Q_R v_R)]$ using $v_R = 2.6\text{ km s}^{-1}$, $Q_R = 1000$. Distances r are great-circle separations from the impact site (35.5°E , 40°S). Peak values in section “Escaped Lunar Ejecta” correspond to the maximum-yield scenario (Crater B on the trailing side). **Science question tags:** **Q1** = Impact dynamics (energy partition, incidence/velocity, ejecta, angles-speeds, escape/recapture, three-body evolution). **Q2** = Lunar interior & response (source time function, attenuation/scattering Q_s , dispersion, crust/megaregolith structure, normal modes). **Q3** = Surface/subsurface materials (thermophysical properties, melt/glass/breccia, volatile retention, boulder SFD, composition links incl. meteorites).

4. OBSERVATION TIMELINE

Given the diversity of physical phenomena predicted—from optical flash to infrared afterglow, seismic shock, and delayed meteoroid flux—a coordinated, multi-platform campaign is essential to capture the 2024 YR₄ lunar impact comprehensively. We have been devoted to apply a systematic analytical framework to the specific 2024 YR₄ lunar impact to probe the Moon as Y. Jiao et al. (2025). Table 2 summarizes all major observables and their detection windows across optical, infrared, seismic, and dynamical domains. Below, we outline an integrated observing strategy following the natural temporal sequence of the event.

In brief, each observable targets distinct science: the optical flash (rise/decay and spectra) constrains kinetic energy, impact angle/velocity, luminous efficiency, and early vapor composition; the NIR/MIR afterglow (cooling curves and maps) probes melt volume, glass/breccia fractions, and regolith thermophysical properties (thermal inertia, porosity, blockiness) under known boundary conditions; broadband seismic wavefields (Rayleigh, body waves, normal modes) recover the source time function and test crust–megaregolith structure, attenuation, scattering, and near-surface layering; orbital imaging and thermal mapping (LROC/Diviner) close the loop on cratering scalings in the km regime, ejecta asymmetry versus obliquity/azimuth, boulder size–frequency distributions, and melt morphology; Earth-adjacent meteoroid flux (mm–cm) diagnoses the high-velocity tail, escape fraction, and the transient cislunar dust environment—also calibrating faint-impact detectability for planetary-defense sensors; meter-class ejecta tracking tests three-body dynamics and radiation-pressure response of fresh lunar boulders while enabling spectroscopy of “lunar-origin mini-asteroids”; secondary lunar impacts measure ejecta recapture efficiency and regolith gardening rates; and recovered meteorites (Fig. 4) provide ground-truth on shock metamorphism, volatile retention, and isotopic/compositional links between the cratered surface, the ejecta field, and small-body provenance.

4.1. Pre-Impact Preparations

Well before the final approach, additional astrometric opportunities will arise that can substantially refine the orbit of 2024 YR₄. In particular, a favorable Earth encounter and observational window around 2028 is expected to enable high-precision optical and radar tracking, significantly reducing uncertainties in the impact probability and corridor on the Moon. These pre-2032 observations will be decisive in confirming whether a lunar impact will occur and in narrowing the predicted

impact geometry to a level suitable for targeted observation planning.

In the months leading to the event, precise refinement of 2024 YR₄’s orbit is critical to constrain the impact corridor and timing to within minutes. Ephemeris refinement will determine which lunar hemisphere and longitude sector to monitor (R. M. Suggs et al. 2008; E. Xilouris et al. 2018; A. Bonanos et al. 2015). Large telescopes (8–10 m class and beyond) can allocate short-term slots around the expected epoch, while networks of medium telescopes (0.3–1 m) with high-speed photometers should plan continuous video coverage to ensure redundancy (M. A. Slade et al. 2010; Z. Ding et al. 2024). On the Moon, active orbiters and landers should be placed in recording or imaging mode, and seismometers armed for immediate data logging. Space agencies can coordinate orbital adjustments of LRO, Chandrayaan-3, or other platforms to enable rapid post-impact passes (B. D. Savage & K. R. Sembach 1996; P. A. Sabelhaus & J. E. Decker 2004; Y. Gong et al. 2019; A. R. Chowdhury et al. 2020).

The predicted impact on 2032-12-22 occurs when the Moon is waning gibbous (~70% illumination). Geometry analysis shows that the southern impact corridor will be visible across the Pacific hemisphere of Earth (G. Merisio & F. Topputo 2023). In particular, the Mauna Kea observatories (Keck, Subaru, Gemini-N) will enjoy optimal visibility with the Moon high (~80°) above the horizon and local pre-dawn darkness. Western North America will see the Moon near dawn at lower elevation, while South America, Europe, and Asia will have daylight or low Moon, rendering the event unobservable from those regions. Thus, coordinated efforts from Hawaii-based facilities, supported by global amateur networks, offer the best chance for optical confirmation.

4.2. Moment of Impact (T_0)

The first seconds are dominated by the optical flash. Observers should begin continuous imaging several minutes prior to the nominal time to capture the rise phase. The expected brightness of $m_V \sim -3$ to -5 makes the event potentially visible to the naked eye if occurring on the lunar night side (with a extremely low probability) (J. M. Madiedo et al. 2019), though contrast against a sunlit surface may reduce detectability but remain strong visibility to hypersensitized telescopes (M. Yanagisawa et al. 2006; J. M. Madiedo et al. 2018). High-speed photometry (10–100 Hz cadence) is essential to resolve the sub-second rise and multi-second decay of the flash. If available, large-aperture telescopes can attempt rapid spectroscopy to identify emission lines of

vaporized silicates or metals. In parallel, orbital imagers (e.g., LROC or small CubeSat payloads) can monitor the near field, while near-infrared facilities could detect the same flash if rapid target-of-opportunity (ToO) observations are enabled.

Even if the impact site lies just beyond the terminator, the event may still illuminate the surrounding terrain or generate Earthshine variations detectable from ground-based photometry.

4.3. Minutes to Hours after T_0

Once the flash fades, the thermal phase begins. Infrared observations should commence within minutes to record the cooling curve of the newly formed ~ 1 km crater. Ground-based mid-IR telescopes (e.g., IRTF, Gemini-North) (L. K. Deutsch et al. 2003) can track the afterglow from ~ 1500 K to a few hundred Kelvins over several hours, while space observatories such as JWST/MIRI can extend this monitoring to longer wavelengths and finer sensitivity (G. Rieke et al. 2015). LRO’s Diviner instrument provides the ideal asset for mapping the temperature evolution and identifying melt deposits (J.-P. Williams et al. 2017; D. A. Paige et al. 2010); follow-up imaging by LROC in the ensuing daylight will reveal the fresh crater morphology and ejecta rays (M. S. Robinson et al. 2010).

Simultaneously, lunar seismometers will register the shock. Rayleigh waves are expected to reach near-side Apollo sites within 7–15 minutes, with predicted peak ground velocities of 10^{-2} – 10^{-1} mm s $^{-1}$ —well above historic Apollo noise levels (R. F. Garcia et al. 2011; J.-F. Blanchette-Guertin et al. 2012). Even farside or polar stations should detect clear arrivals, offering a rare opportunity to probe the Moon’s crustal structure using a known energy source.

Finally, lunar seismic records from all stations will be analyzed to reconstruct source parameters, verify energy coupling efficiency, and refine models of lunar interior structure. The 2024 YR₄ impact, if it occurs, would thus provide a complete multi-modal dataset: optical and infrared emissions tracing energy release, seismic waves probing the interior, and orbital imaging revealing geological consequences—a natural experiment in planetary impact physics.

4.4. Days to Years after T_0

In the following days, attention shifts from immediate transients to slower processes and byproducts. As the impact site rotates into sunlight, lunar orbiters should obtain high-resolution optical imaging to measure the final crater dimensions and ejecta albedo. On Earth, meteor and radar networks should monitor for

a transient increase in meteoroid flux roughly 2–8 days post-impact, corresponding to lunar ejecta fragments reaching Earth’s vicinity. These fragments—typically mm–cm in size—could produce a short-lived meteor shower radiating from the Moon’s orbital direction.

The first month after T_0 is the high-yield window for targeted campaigns. Accordingly, ground-based meteor cameras and high-power radars should maintain near-continuous coverage from T_0+2 to T_0+10 days to capture the early peak in the trailing-side cases, then intensify cadence around T_0+30 and T_0+90 days for secondary peaks. For leading-side impacts, the same infrastructure should pivot to a deferred campaign starting near T_0+80 days and extending for several weeks, with expectations set for lower but detectable flux.

We recommend a tiered follow-up: wide-field discovery and alert brokering; rapid astrometric recovery with 2–4 m telescopes to refine orbits; prompt low-resolution reflectance spectroscopy on 4–10 m class telescopes to test lunar provenance; and, where feasible, deep photometry or thermal IR (including space assets) to constrain size, albedo, and surface state. More specific observing classification has been listed in M. Devogèle et al. (2025).

A small but predictable fraction of escapees should reimpact the Moon with inter-peak spacings near the synodic period, favoring early-time returns (first few tens of days), which implies a relatively well-defined observation window for more concentrated observing resources. Although individual flashes are faint, a few-day continuous monitoring campaign around predicted windows—using existing lunar flash detection networks and small telescopes pointed to the appropriate selenographic longitudes—can directly test ejecta recapture physics and constrain the near-Moon particulate environment.

Model-guided recovery of lunar meteorites is also warranted. Orbit integrations coupled to size–velocity distributions predict that a small but non-negligible fraction of escaping fragments survive atmospheric entry as meteorites within the first two years. For trailing-hemisphere (east-longitude) impacts, the bulk of the delivery occurs within the first year with an order-of-magnitude cumulative mass in the 10^1 – 10^2 kg range and an upper envelope reaching a few $\times 10^2$ kg under high-yield realizations; for leading-hemisphere (west-longitude) impacts, arrivals are delayed (commencing near T_0+80 days) and the integrated mass is lower by a factor of a few. Figure 4 summarizes these outcomes by showing the predicted global distribution of surviving meteorite mass delivered to Earth over the first two years following the impact (T_0 to T_0+2 yr). For each of the six representative source craters, the panels map the

cumulative recovered mass (kg) within equal-area geographic grid cells projected onto a standard world map. In all cases, the surviving mass is preferentially delivered to low- and mid-latitudes (typically within $\pm 30^\circ$), with broad longitudinal coverage reflecting Earth's rotation during debris interception. This geographic concentration implies that coordinated, regionally targeted recovery strategies—combining global meteor networks for trajectory reconstruction with rapid-response ground searches—can substantially enhance the probability of meteorite recovery. Fresh lunar meteorites from this event would anchor laboratory studies of regolith thermophysics and shock metamorphism and provide a compositional cross-check against remotely sensed spectra, directly linking the surface, the ejecta dynamics, and samples in hand.

As indicated in Section 3.4.4, the year following the 2024 YR₄ impact offers a unique window to monitor tens to hundreds of observable meter- and sub-meter-sized lunar ejecta. While significantly smaller than typical observable Near-Earth Objects (NEOs), these boulders possess substantial mass. Crucially, the majority remain bound to Earth, implying close proximity and low relative velocities. This accessibility presents two time-sensitive opportunities that warrant immediate mission planning:

1. Sample Retrieval: Capturing and maneuvering these fragments into stable geocentric orbits is feasible (H.-X. Baoyin et al. 2010), allowing for the retrieval of massive samples originating from the lunar interior.
2. Planetary Defense: These optimally sized targets serve as ideal testbeds for low-cost validation of defense technologies, such as conducting realistic kinetic impact experiments (Y. Jiao et al. 2023; K. Lee et al. 2025b,a).

5. CONCLUSION

If the potential lunar impact of asteroid 2024 YR₄ indeed occurs, it would produce an exceptionally bright, multi-modal signal and a once-in-10⁴-year natural experiment on the Moon. According to our modeling, we may then expect an optical/NIR flash reaching $m_V \sim -3$

over $\sim 10^2$ – 10^3 s with $T_{\text{eff}} \sim 1.8$ – 2.3×10^3 K, a global $M \sim 5$ moonquake, a km-scale fresh crater, and a total mass of 10^7 – 10^8 kg of high-velocity ejecta linking the lunar surface to cislunar space. These predictions finally yield a single, time-ordered plan from the first seconds to the following weeks.

Beyond establishing the detectability, this event unlocks a broad science return that is rarely available in planetary science: (1) the surface and near-surface thermophysics under known boundary conditions (flash spectra, melt-pool cooling, Diviner-class thermal mapping); (2) the interior structure and attenuation from a calibrated, high-S/N Rayleigh-wave source recorded by modern stations (e.g., polar and farside packages), enabling joint inversions with legacy Apollo constraints; (3) the hypervelocity cratering, the energy coupling, and the oblique-impact ejecta systematics at kilometer scale for testing scaling laws and numerical models; and (4) source-tagged dust and meteoroids that trace regolith–exosphere exchange and deliver lunar material to near-Earth space—linking small-body provenance, lunar meteorites, and operational space-safety questions.

Practically, our results provide a clear picture of the cross-platform campaign: high-speed photometry and rapid spectroscopy at T_0 ; hours-to-days mid-IR monitoring of the afterglow; immediate, networked seismic acquisition for global arrivals; rapid-response orbital imaging and thermal mapping; and short-lag radar/meteor surveillance for escaped ejecta. If the collision indeed happens, the 2024 YR₄ impact will become the brightest and best-characterized lunar impact on record and also a benchmark for impact and hazard models. If it does not, the methodology, visibility analysis, and coordination logic presented here remain a reusable blueprint for rapid-response observations of future natural impacts—turning potential hazard into preparedness and, ultimately, into discovery.

ACKNOWLEDGMENTS

This work is supported by the National Natural Science Foundation of China under Grant Nos. 12572404, 62227901, U24B2048, 125B1015, 123B2038, the national level fund No. KJSP2023020301, the Beijing Nova Program No. 20250484831, and the Tsinghua Dushi Funds.

REFERENCES

Ait Moulay Larbi, M., Daassou, A., Baratoux, D., et al. 2015, *Earth, Moon, and Planets*, 115, 1

Aki, K., & Richards, P. G. 2002, Quantitative seismology

Baoyin, H.-X., Chen, Y., & Li, J.-F. 2010, *Research in Astronomy and Astrophysics*, 10, 587

Blanchette-Guertin, J.-F., Johnson, C. L., & Lawrence, J. F. 2012, *Journal of Geophysical Research: Planets*, 117

Bolin, B. T., Hanuš, J., Denneau, L., et al. 2025, *The Astrophysical Journal Letters*, 984, L25

Bonanos, A., Xilouris, M., Boumis, P., et al. 2015, *Proceedings of the International Astronomical Union*, 10, 327

Bouley, S., Baratoux, D., Vaubaillon, J., et al. 2012, *Icarus*, 218, 115

Burns, J. A., Lamy, P. L., & Soter, S. 1979, *Icarus*, 40, 1, doi: [10.1016/0019-1035\(79\)90050-2](https://doi.org/10.1016/0019-1035(79)90050-2)

Ceplecha, Z., Borovička, J., Elford, W. G., et al. 1998, *Space Science Reviews*, 84, 327

Cheng, B., & Baoyin, H. 2024, *Monthly Notices of the Royal Astronomical Society*, 534, 1376

Cheng, B., Yu, Y., & Baoyin, H. 2018, *Physical Review E*, 98, 012901

Chowdhury, A. R., Banerjee, A., Joshi, S., et al. 2020, *Current Science*, 118, 368

Collins, G., Elbeshausen, D., Davison, T., Robbins, S., & Hynek, B. 2011, *Earth and Planetary Science Letters*, 310, 1

Collins, G. S., Melosh, H. J., & Ivanov, B. A. 2004, *Meteoritics & Planetary Science*, 39, 217

Deutsch, L. K., Hora, J. L., Adams, J. D., & Kassis, M. 2003, in *Instrument Design and Performance for Optical/Infrared Ground-based Telescopes*, Vol. 4841, SPIE, 106–116

Devogèle, M., Hainaut, O. R., Micheli, M., et al. 2025, arXiv preprint arXiv:2511.09405

Ding, Z., Zhu, K., Dong, Z., Li, L., & Zeng, T. 2024, in *EUSAR 2024; 15th European Conference on Synthetic Aperture Radar*, VDE, 1004–1007

Garcia, R. F., Gagnepain-Beyneix, J., Chevrot, S., & Lognonné, P. 2011, *Physics of the Earth and Planetary Interiors*, 188, 96

Gong, Y., Liu, X., Cao, Y., et al. 2019, *The Astrophysical Journal*, 883, 203

Gudkova, T., Lognonné, P., & Gagnepain-Beyneix, J. 2011, *Icarus*, 211, 1049

Ivezić, Ž., Kahn, S. M., Tyson, J. A., et al. 2019, *The Astrophysical Journal*, 873, 111, doi: [10.3847/1538-4357/ab042c](https://doi.org/10.3847/1538-4357/ab042c)

Jiao, Y., Cheng, B., & Baoyin, H. 2023, *Journal of Guidance, Control, and Dynamics*, 46, 382, doi: [10.2514/1.G006876](https://doi.org/10.2514/1.G006876)

Jiao, Y., Cheng, B., & Baoyin, H. 2025, arXiv preprint arXiv:2509.01436

Jiao, Y., Yan, X., Cheng, B., & Baoyin, H. 2024a, *Monthly Notices of the Royal Astronomical Society*, 527, 10348, doi: [10.1093/mnras/stad3888](https://doi.org/10.1093/mnras/stad3888)

Jiao, Y., Cheng, B., Huang, Y., et al. 2024b, *Nature Astronomy*, 8, 819, doi: [10.1038/s41550-024-02258-z](https://doi.org/10.1038/s41550-024-02258-z)

Jutzi, M. 2015, *Planetary and space science*, 107, 3

Jutzi, M., Benz, W., & Michel, P. 2008, *Icarus*, 198, 242

Jutzi, M., Michel, P., Hiraoka, K., Nakamura, A. M., & Benz, W. 2009, *Icarus*, 201, 802

Lee, K., Baoyin, H., & Wang, Z. 2025a, *Acta Astronautica*

Lee, K., Fang, Z., & Wang, Z. 2025b, *Icarus*, 425, 116312, doi: [10.1016/j.icarus.2024.116312](https://doi.org/10.1016/j.icarus.2024.116312)

Liu, X., Hou, X., & Cheng, H. 2025, *npj Space Exploration*, 1, 4

Luo, X.-Z., Zhu, M.-H., & Ding, M. 2022, *Journal of Geophysical Research: Planets*, 127, e2022JE007333

Madiedo, J. M., Ortiz, J. L., & Morales, N. 2018, *Monthly Notices of the Royal Astronomical Society*, 480, 5010

Madiedo, J. M., Ortiz, J. L., Morales, N., & Cabrera-Caño, J. 2014, *Monthly Notices of the Royal Astronomical Society*, 439, 2364

Madiedo, J. M., Ortiz, J. L., Morales, N., & Santos-Sanz, P. 2019, *Monthly Notices of the Royal Astronomical Society*, 486, 3380

Madiedo, J. M., Ortiz, J. L., Organero, F., et al. 2015, *Astronomy & Astrophysics*, 577, A118

Marvin, U. B. 1983, *Geophysical Research Letters*, 10, 775

Melosh, H. 1989, *Press*, New York

Merisio, G., & Topputo, F. 2023, *Icarus*, 389, 115180

Minor Planet Center. 2024, *MPEC 2024-Y140: 2024 YR4*, <https://www.minorplanetcenter.net/mpec/K24/K24YE0.html>

NASA. 2025, *NASA's Webb Observations Update Asteroid 2024 YR4's Lunar Impact Odds*, <https://science.nasa.gov/blogs/planetary-defense/2025/06/05/nasas-webb-observations-update-asteroid-2024-yr4s-lunar-impact-odds/>

NASA/JPL Small-Body Database. 2025, *2024 YR4, Small-Body Database Lookup*, https://ssd.jpl.nasa.gov/tools/sbdb_lookup.html#/?sstr=2024%20YR4

Nunn, C., Fernando, B. A., & Panning, M. P. 2024, *The Planetary Science Journal*, 5, 246

Nunn, C., Garcia, R. F., Nakamura, Y., et al. 2020, *Space Science Reviews*, 216, 89

Paige, D. A., Siegler, M. A., Zhang, J. A., et al. 2010, *science*, 330, 479

Popova, O., Borovička, J., Hartmann, W. K., et al. 2011, *Meteoritics & Planetary Science*, 46, 1525

Rein, H., & Liu, S.-F. 2012, *Astronomy & Astrophysics*, 537, A128, doi: [10.1051/0004-6361/201118085](https://doi.org/10.1051/0004-6361/201118085)

Rieke, G., Ressler, M., Morrison, J. E., et al. 2015, *Publications of the Astronomical Society of the Pacific*, 127, 665

Rivkin, A., Mueller, T., MacLennan, E., et al. 2025, *Research Notes of the AAS*, 9, 70

Robinson, M. S., Brylow, S., Tschimmel, M. e., et al. 2010, *Space science reviews*, 150, 81

Sabelhaus, P. A., & Decker, J. E. 2004, Optical, Infrared, and Millimeter Space Telescopes, 5487, 550

Sato, H., Fehler, M. C., & Maeda, T. 2012, Seismic wave propagation and scattering in the heterogeneous earth, Vol. 496 (Springer)

Savage, B. D., & Sembach, K. R. 1996, *Annual Review of Astronomy and Astrophysics*, 34, 279

Slade, M. A., Benner, L. A., & Silva, A. 2010, *Proceedings of the IEEE*, 99, 757

Subasinghe, D., & Campbell-Brown, M. 2018, *The Astronomical Journal*, 155, 88

Suggs, R. M., Cooke, W. J., Suggs, R. J., Swift, W. R., & Hollon, N. 2008, *Earth, Moon, and Planets*, 102, 293

Wiegert, P., Brown, P., Lopes, J., & Connors, M. 2025, *ApJL*, 990, L20, doi: [10.3847/2041-8213/adfa8b](https://doi.org/10.3847/2041-8213/adfa8b)

Williams, J.-P., Paige, D., Greenhagen, B., & Sefton-Nash, E. 2017, *Icarus*, 283, 300

Wu, Y., Jiao, Y., Dai, W.-Y., et al. 2025, arXiv preprint arXiv:2510.23155

Xilouris, E., Bonanos, A., Bellas-Velidis, I., et al. 2018, *Astronomy & Astrophysics*, 619, A141

Yanagisawa, M., Ohnishi, K., Takamura, Y., et al. 2006, *Icarus*, 182, 489

Yu, Y., Michel, P., Schwartz, S. R., Naidu, S. P., & Benner, L. A. 2017, *Icarus*, 282, 313